Supporting Information

Oxygen Vacancies Mediated WO_3 Nanosheets by Etched {200} Facets and the Efficient Visible-light Photocatalytic Oxygen Evolution

Yurong Yang,*[a,b] Jiaming Chen,[a] Xuelian Liu,[a] Min Qiu,[a] Li Liu,[a] and Fan Gao[a]

[a] College of Science, Heihe University, Heihe, Heilongjiang 164300, (P. R. China), e-mail: yangyurong@hrbeu.edu.cn

[b] Key Laboratory of Superlight Materials and Surface Technology, Ministry of Education, College of Materials Science and Chemical Engineering, Harbin Engineering University, Harbin, Heilongjiang, 150001 (P. R. China), e-mail: yangyurong@hrbeu.edu.cn

Characterization

X-ray diffraction (XRD) patterns of the samples were recorded by a D/MAX2500 diffractometer equipped with Cu Kα radiation (λ=0.15406 nm). Diffraction patterns were collected from 10° to 70° at a scan rate of 10 ^{o}C min^{-1}. The field emission scanning electron microscopy (FE-SEM) images were taken on a SU8000 cold emission field scanning electron microanalyser (Hitachi, Japan). Transmission electron microscopy (TEM), high-resolution transmission electron microscopy (HRTEM) experiments were performed on a JEOL 2010 transmission electron microscope with a field emission gun operated at 200 kV. Raman spectroscopic analysis of the samples were performed by using a micro-Raman system with an Ar ion laser 488 nm, and a probing laser 50 W cm^{-2} was guided during the illumination. X-ray photoelectron spectroscopy (XPS) examination were performed by using a PHI 5700 ESCA System with a monochromatic Al Kα (1486.6 eV) radiation source and a hemisphere detector. The ultraviolet–visible diffuse reflectance spectrum (UV-vis DRS) measurements were conducted using a UV-vis spectrophotometer (Shimadazu, UV-2550) with $BaSO_4$ as the reference sample. Brunauer-Emmett-Teller (BET) nitrogen adsorption-desorption measurements (Micromeritics TriStar 3020) were carried out to determine the as-prepared samples' specific surface area at 77 K. The steady-state photoluminescence (PL) spectrum were measured using a spectrophotometer (Jobin Yvon Fluorolog 3-221) with a Xe lamp (450 W) as excitation source at the excitation wavelength of 365 nm. The time-resolved decay curves of the samples were tested using a fluorescence lifetime spectrophotometer (FLS920, Edinburgh Instruments, UK) under the excitation wavelength of 365 nm. (Zeta potential distribution measurements were performed on a ZEN3690 Zetasizer Nano detector (Malven, UK). The electron paramagnetic reso-nance (EPR) spectra were recorded on a Bruker EPR EMX-10/12 X-band spectrometer. The contact angles were investigated

by a contact angle measurement device equipped with a side camera (IDS uEye camera) and a goniometer. The interface between the surface and the water drop was more precisely characterized by laser scanning confocal microscopy (LSCM, Leica Microsystems TCS SP8). Zeta potential distribution was performed on a ZEN3690 Zetasizer Nano detector (Malven, UK). The magnetic property of the samples were measured by vibrating sample magnetometer (VSM, Lake Shore M7407).

The average lifetime could be calculated according to the following equation:

$$\tau_{ave.} = \frac{A_1\tau_1^2 + A_2\tau_2^2 + A_3\tau_3^2}{A_1\tau_1 + A_2\tau_2 + A_3\tau_3} \quad (1)$$

Where τ_1, τ_2 and τ_3 are the emission lifetimes, and A_1, A_2 and A_3 are the corresponding amplitudes.

Photo-electrochemical measurements

1.0 mg as-prepared sample was dispersed in 1 mL ethanol, and then it was uniformly spin-dropped onto a 1 cm×1 cm FTO glass substrate by a spin coater (VTC-50A, China). Subsequently, the glass was heated at 60 ^{o}C in a vacuum oven for 10 hours.

The photocurrent measurements were recorded on a semiconductor characterization system (Keithley 4200 SCS) with a Lakeshore probe station and a xenon lamp (300 W, λ>400 nm) was used as the visible-light source.

Electrochemical impedance spectroscopy measurements were performed on a CHI 660D electrochemical station (Shanghai Chenhua) with a three-electrode system, in which Pt foil and saturated Ag/AgCl were used as the counter electrode and reference electrode, respectively. And the electrolyte was 1 M Na_2SO_4 solution bubbled with N_2 for 30 min before the measurements.

O_2 evolution measurement

The photocatalytic O_2 production experiments were performed in a top-irradiation quartz flat-bottom container (500 mL) connected to a closed gas circulation system. Firstly 50 mg catalyst powder was dispersed in a 100 mL aqueous solution of 10 mM silver nitrate solution. A 300 W xenon arc lamp (CEL-HXF300, Beijing, China) was used as a visible light source to trigger the photocatalytic reaction. The power density of the incident light was 180 mW cm^{-2}, which was measured by a CEL-HFX300 Visible spectrophotometer. The amount of O_2 evolution was measured using an on-line gas chromatograph (SP7800, TCD, molecular sieve 0.5 nm, Ar carrier, Beijing Keruida Limited).

The apparent quantum efficiency (QE) was determined under the same photocatalytic reaction condition except that a 420 nm xenon arc lamp was used as light source to trigger the photocatalytic reaction. The QE was calculated by the following Equation:

$$\mathrm{QE} = \frac{\text{number of reacted electrons}}{\text{number of incident photons}} \times 100\%$$

$$= \frac{\text{number of evolved } O_2 \text{molecules} \times 4}{\text{number of incident photons}} \times 100\%$$

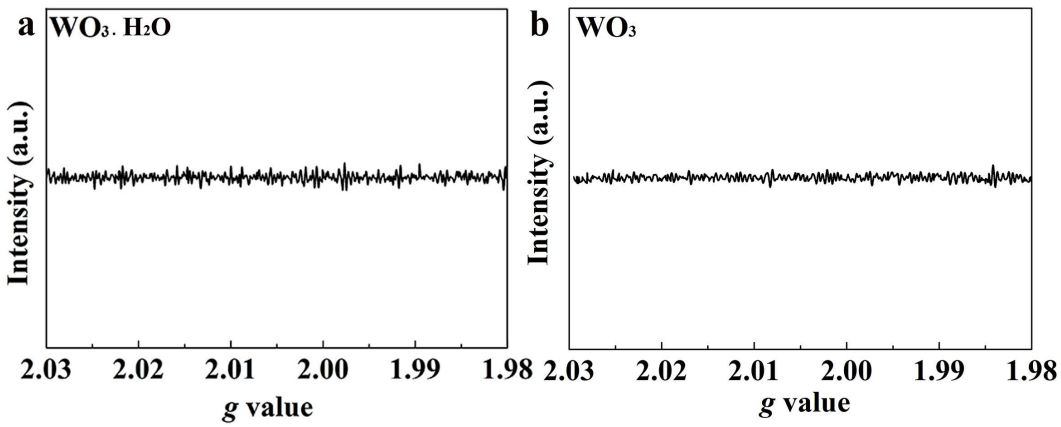

Figure S1. A direct Z-scheme system of $WO_3.H_2O$/g-C_3N_4.

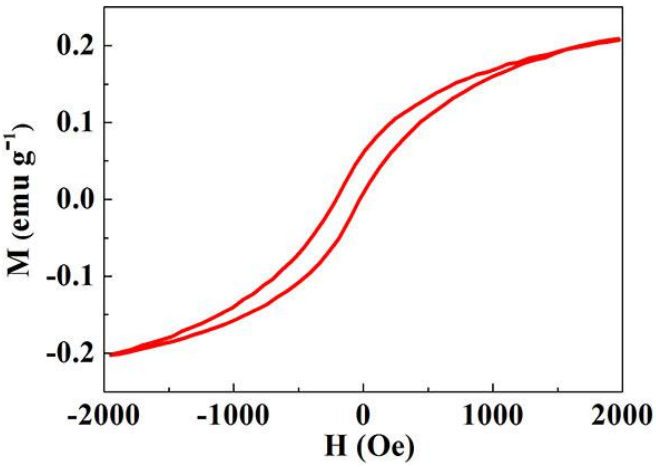

Figure S2. Magnetic field dependence of magnetization of WO_{3-x}.

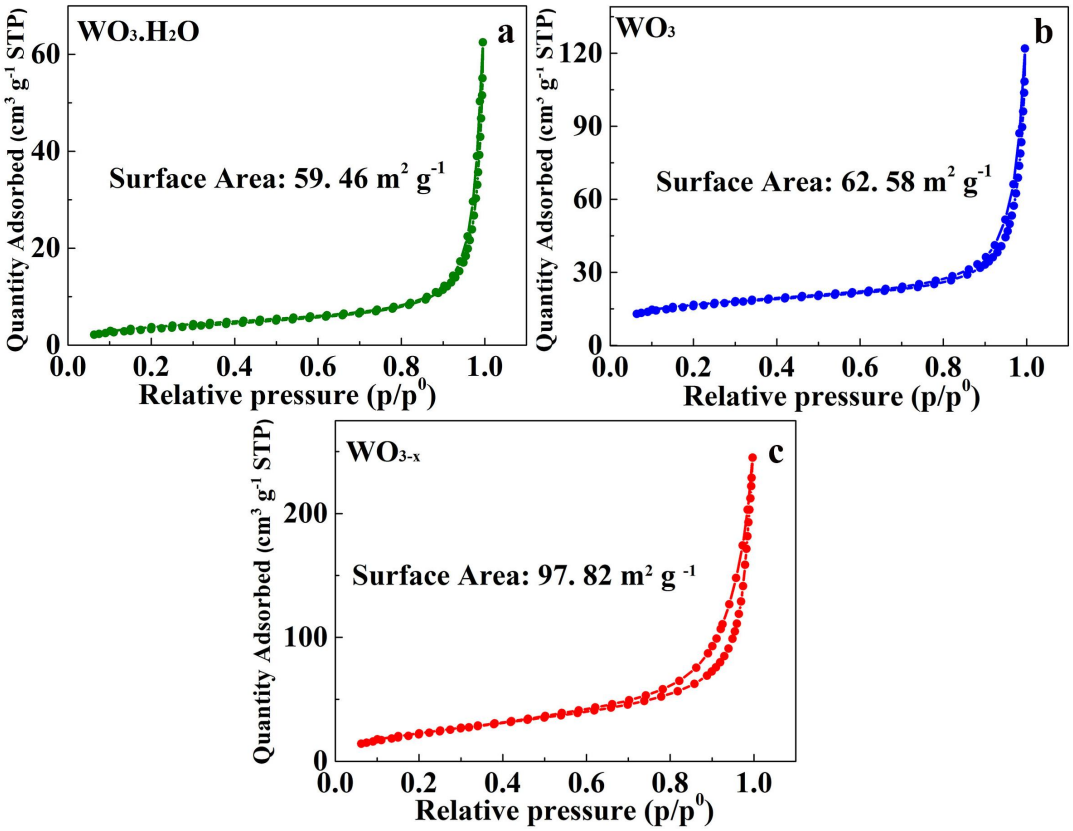

Figure S3. Nitrogen absorption-desorption isotherms of (a) $WO_3.H_2O$ (b) WO_3 and (c) WO_{3-x}.

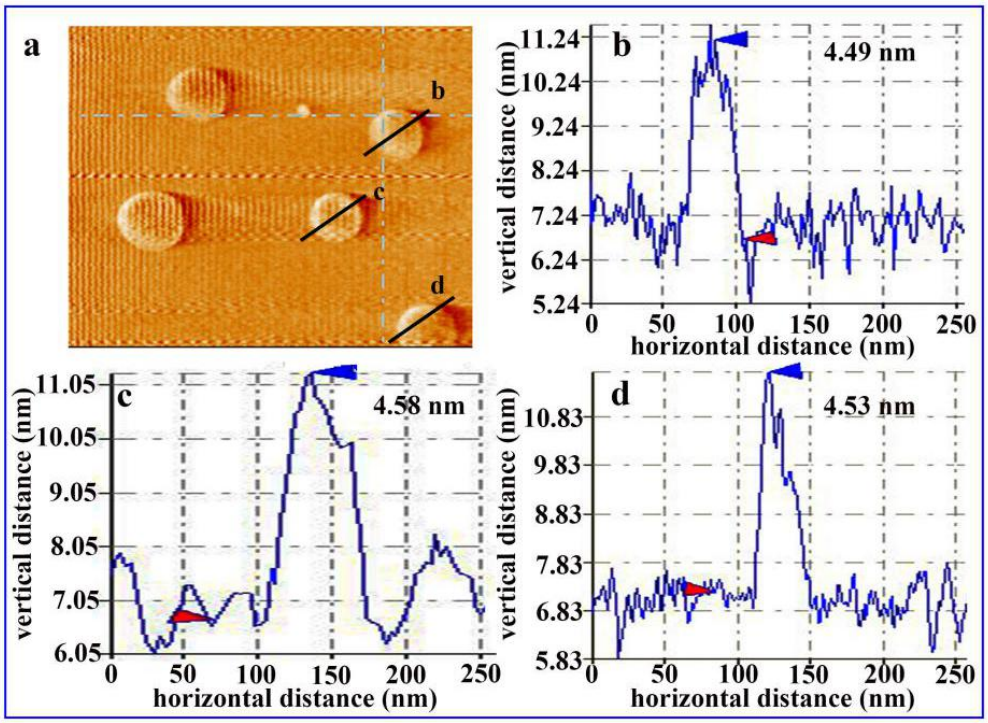

Figure S4. (a) AFM image of the WO_3 nanosheets; (b-d) The vertical distance and horizontal distance information of different nanosheets from the AFM images.

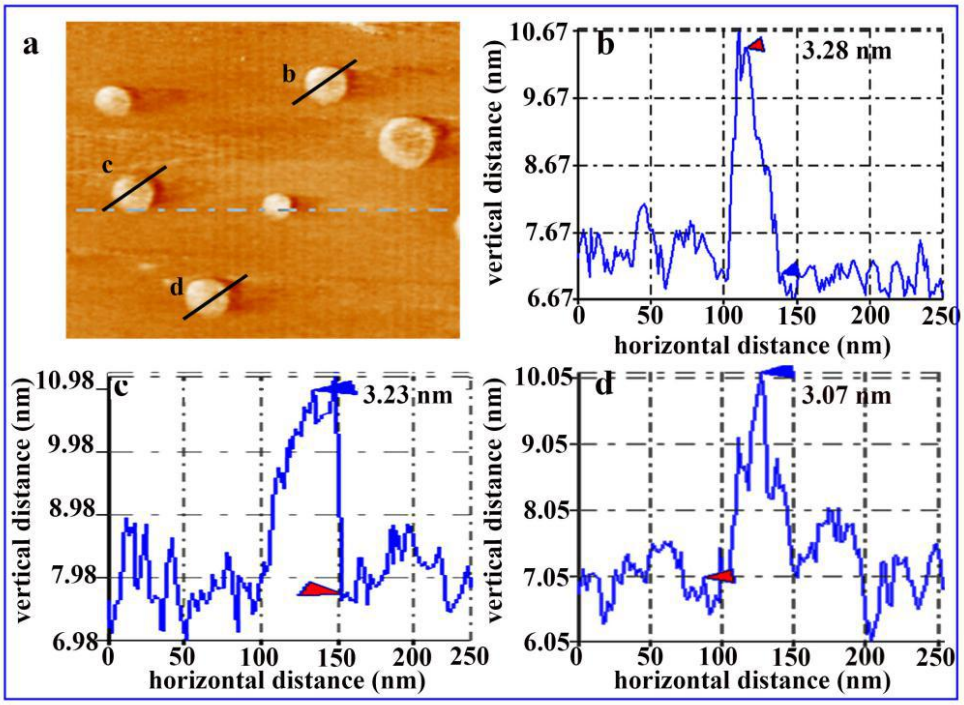

Figure S5. (a) AFM image of the WO_{3-x} nanosheets; (b-d) The vertical distance and horizontal distance information of different nanosheets from the AFM images.

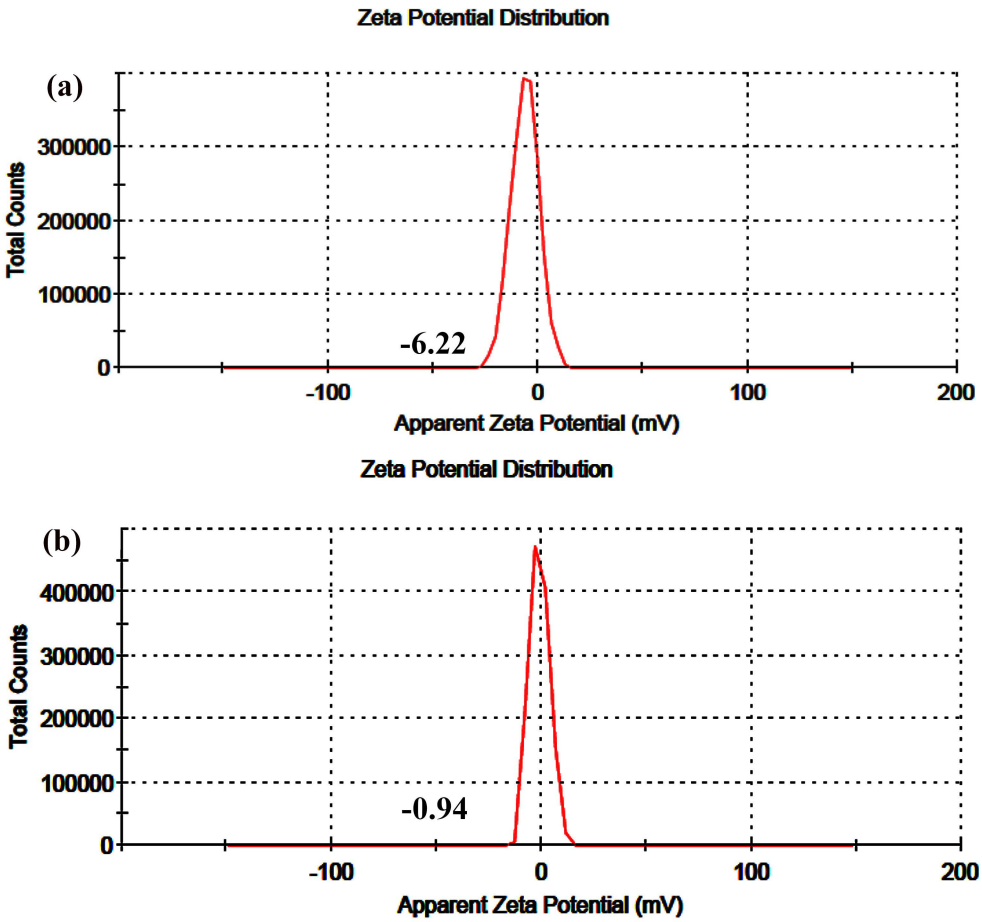

Figure S6. Zeta potential of WO_{3-x} (a) and WO_3 nanosheets (b).

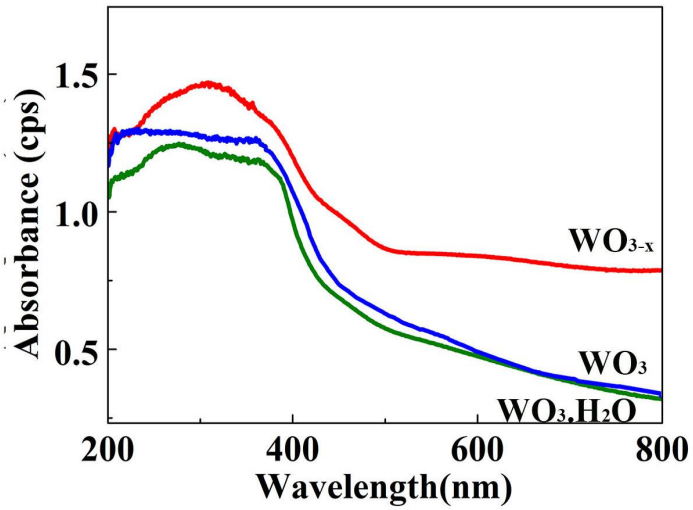

Figure S7. UV-vis DRS of the $WO_3.H_2O$, WO_3 and WO_{3-x} nanosheets.

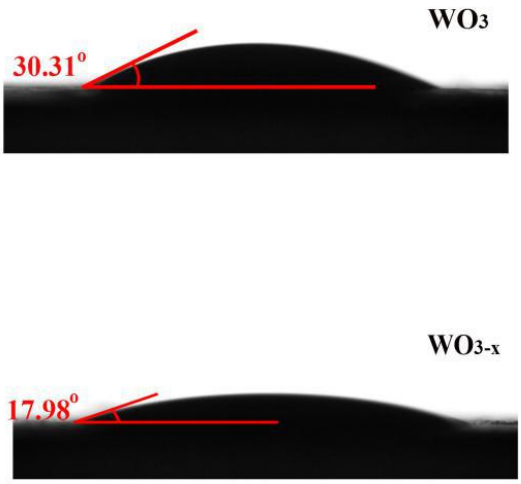

Figure S8. Side-view image of a water drop on the WO_3 and WO_{3-x} nanosheets surface.

In order to prove that the favored charge separation induced by this appropriate amount of Ov, WO_{3-x} nanosheets with different content of Ov were prepared by a simple hydrothermal etching except that the amount of NH_4HF_2, the obtained products were named as L-WO_{3-x} and F-WO_{3-x}, respectively. As shown in Figure S10, when adding a little NH_4HF_2 aqueous solution (0.1 M, 30 mL), a weak signal of the Ov is detected in the L-WO_{3-x} nanosheets. However, after adding more NH_4HF_2 aqueous solution (0.2 M, 30 mL), it is clearly observed a strong and broad characteristic peak. Generally, the bigger Ov peak area indicates the more Ov exist in the sample.[33] Combining with EPR spectra of the WO_{3-x} nanosheets, it is found that the content of Ov in the sample turn out to be in the order of L-WO_{3-x} < WO_{3-x} < F-WO_{3-x}. Furhermore, photocatalytic oxygen activity of the L-WO_{3-x} and F-WO_{3-x} nanosheets are measured under simulated solar light. As shown in Figure S11, the photocatalytic oxygen evolution rate for L-WO_{3-x} and F-WO_{3-x} nanosheets is approximately 98 and 169 μmol h^{-1} g^{-1} respectively, which are much lower than that of the WO_{3-x} nanosheets (378 μmol h^{-1} g^{-1}). Therefore, with the content of the Ov increasing, the photocatalytic activity of the sample firstly increases and then decreases. This suggests that introducing an appropriate amount of Ov in WO_3 nanosheets can provides the sample with less trapping centers and prolongs retention of carriers, as well as enhanced photocatalytic activity. Meanwhile, excessive Ov forms the recombination sites for photogenerated charges.

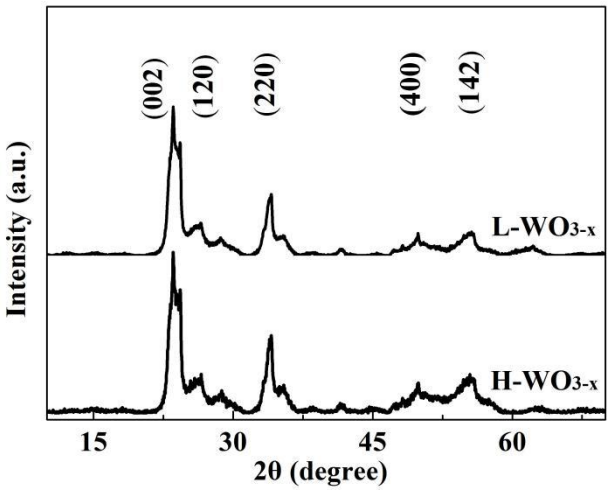

Figure S9. XRD patterns of the L-WO_{3-x} and F-WO_{3-x} nanosheets.

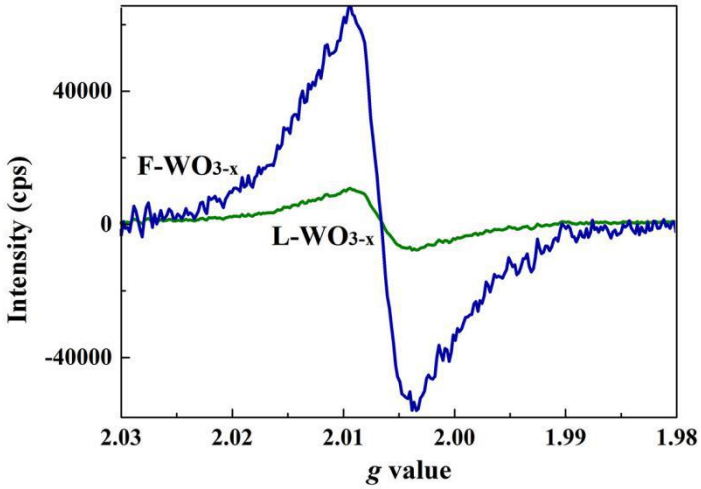

Figure S10. EPR spectra of the L-WO_{3-x} and F-WO_{3-x} nanosheets.

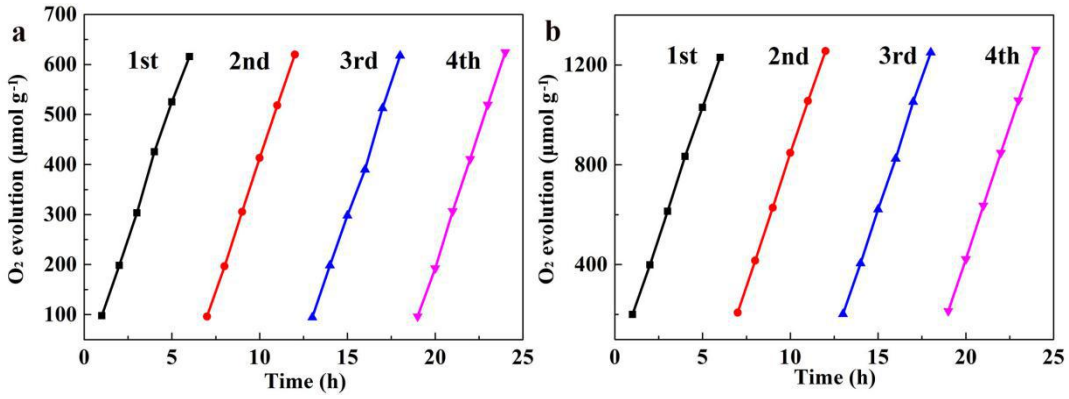

Figure S11. Simulated solar light driven photocatalytic O_2 production for the L-WO_{3-x} nanosheets (a) and F-WO_{3-x} nanosheets (b).

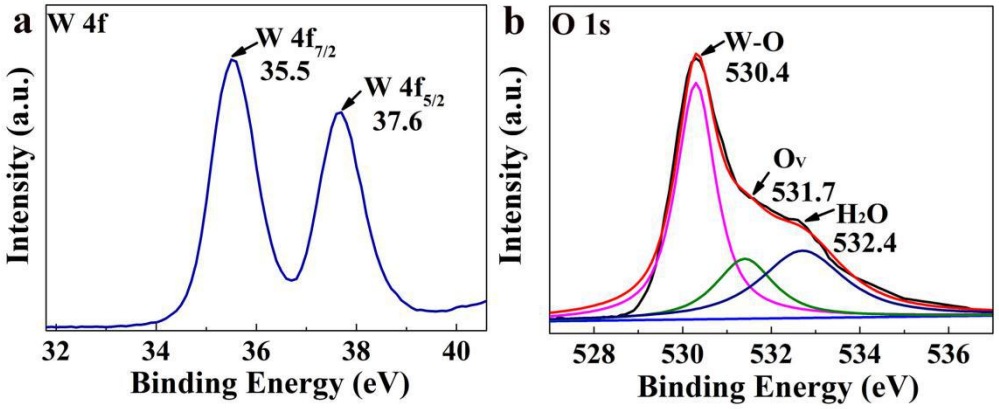

Figure S12. (a) W 4f and (b) O 1s XPS spectra for the WO_{3-x} nanosheets after photocatalytic O_2 production.

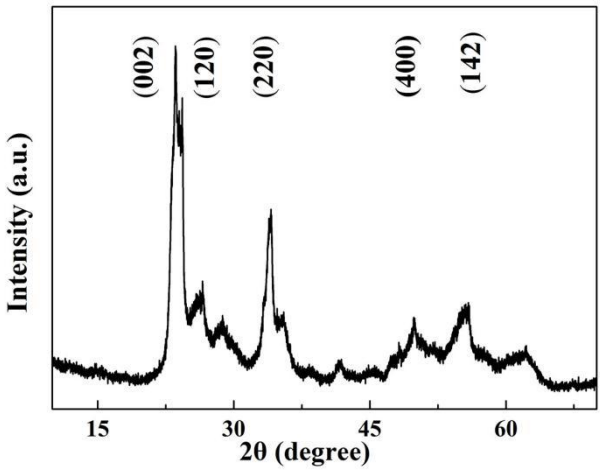

Figure S13. XRD patterns of the WO_{3-x} nanosheets after photocatalytic O_2 production.

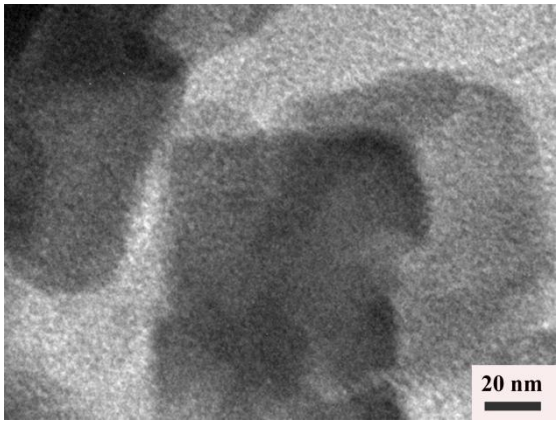

Figure S14. TEM image of the WO_{3-x} nanosheets after photocatalytic O_2 production.

Table S1. The fitted parameters obtained from decay curves of WO_3 and WO_{3-x} nanosheets.

Sample	τ_1 (ns)	α_1 (%)	τ_2 (ns)	α_2 (%)	τ_3 (ns)	α_3 (%)	$\tau_{ave.}$ (ns)	χ^2
WO_3	0.94	35.44	4.82	54.50	21.02	10.06	11.32	1.536
WO_{3-x}	2.37	39.96	7.21	49.37	53.40	10.67	32.55	1.588